Journal of Power Sources 195 (2010) 4149–4159

Contents lists available at ScienceDirect

Journal of Power Sources

journal homepage: www.elsevier.com/locate/jpowsour

Coupled modeling of water transport and air–droplet interaction in the electrode of a proton exchange membrane fuel cell

Angelo Esposito[a,b], Cesare Pianese[a,*], Yann G. Guezennec[b]

[a] Department of Mechanical Engineering, University of Salerno, via Ponte Don Melillo 1, 84084 Fisciano (SA), Italy
[b] Center for Automotive Research, The Ohio State University, 930 Kinnear Rd, Columbus, 43212 OH, USA

ARTICLE INFO

Article history:
Received 17 July 2009
Received in revised form 26 October 2009
Accepted 10 January 2010
Available online 18 January 2010

Keywords:
PEMFC control
Design and diagnosis
Liquid water transport
Water droplets formation
Growth
Coalescence and detachment

ABSTRACT

In this work, an accurate and computationally fast model for liquid water transport within a proton exchange membrane fuel cell (PEMFC) electrode is developed by lumping the space-dependence of the relevant variables. Capillarity is considered as the main transport mechanism within the gas diffusion layer (GDL). The novelty of the model lies in the coupled simulation of the water transport at the interface between gas diffusion layer and gas flow channel (GFC). This is achieved with a phenomenological description of the process that allows its simulation with relative simplicity. Moreover, a detailed two-dimensional visualization of such interface is achieved via geometric simulation of water droplets formation, growth, coalescence and detachment on the surface of the GDL. The model is useful for optimization analysis oriented to both PEMFC design and balance of plant. Furthermore, the accomplishment of reduced computational time and good accuracy makes the model suitable for control strategy implementation to ensure PEM fuel cells operation within optimal electrode water content.

1. Introduction

A PEM fuel cell has a sandwich structure with a polymeric membrane enclosed between two porous electrodes (Fig. 1). The membrane is an electric insulator, is gas impermeable and is an excellent proton conductor if properly humidified. When hydrogen and oxygen, or air, are fed to the anode and cathode respectively, electrons are released by hydrogen, go along an external circuit and reach the anode side, where they combine with oxygen and protons, which flow through the polymeric membrane, to form water. A difference in the electrochemical potential sets up across the cell and is available to an external load. However, the correct operation of a PEMFC is guaranteed only if the polymeric membrane water content ranges between well defined limits. The proton conductivity is indeed directly related to the membrane humidification level.

PEMFC electrodes include a porous media, often called gas diffusion layer (GDL) and a platinum catalyst. Although there have been recent studies on the potential application of carbon nanostructures as diffusion media [1,2], the most common used GDLs have a porous structure made of carbon paper or cloth, pre-treated with PTFE. They promote the diffusion of reactants from gas channels to the catalyst and excess of water (generated by the reaction or coming from the electrolyte) into the opposite direction. Moreover, gas diffusion layers represent a mechanical support for the cell and form an electrical and thermal connection between external plates and the catalyst. The electrode can experience the undesired flooding phenomenon, that occurs when the pores of the material are filled up with liquid water. A gas diffusion layer may be flooded under operating conditions such as: high current densities, high reactant humidity, low gas flow rates, low temperature or a combination thereof. It results in an occlusion of the pores that hinders the gas diffusion to the catalyst layer, causing worse cell performance and shut-off in the worst case. A lower than ideal concentration of reacting gases at the catalyst sites decreases the number of chemical reactions at the electrodes reducing the effectiveness of the reaction sites. Likewise, an excess of product water hinders the diffusion of the reacting gases reducing the reaction rate.

In light of the above described phenomena, it is important to consider that the two-phase water balance inside the electrode of a PEMFC is a determinant factor to guarantee cell performance and reliable and lifelong operations. Performance optimization can be achieved by combining proper cell design with appropriate control strategies. It is indeed necessary to balance the water concentration of all streams in and out of a fuel cell to guarantee proper membrane humidification. Such a balance depends on water generation and transport mechanisms within each cell. In particular, the liquid water transport is strongly affected by the air flow–water (vapor or

* Corresponding author. Tel.: +39 089 96 4081; fax: +39 089 96 4037.
E-mail addresses: angesposito@unisa.it (A. Esposito), pianese@unisa.it (C. Pianese), guezennec.1@osu.edu (Y.G. Guezennec).

0378-7753/$ – see front matter © 2010 Elsevier B.V. All rights reserved.
doi:10.1016/j.jpowsour.2010.01.020

Nomenclature

Nomenclature

A	surface area (cm^2)
A_d	droplet cross-sectional area (m^2)
c	droplet chord (m)
C	concentration ($mol\,m^{-3}$)
D	droplet diameter (m)
D_w	membrane water diffusion coefficient ($m^2\,s^{-1}$)
F	Faraday constant (96,485 C (equiv. mol)$^{-1}$)
h	droplet height (m)
H	GFC height (m)
i	current density ($A\,cm^{-2}$)
k_m	mass transfer coefficient ($m\,s^{-1}$)
k_r	relative permeability
K	absolute permeability (m^2)
l	thickness (m)
m	mass (kg)
M	molecular weight ($kg\,mol^{-1}$)
N	number of GFCs in parallel
N_{drop}	number of droplets at the interface
n_d	electro-osmotic drag coefficient
P	pressure (Pa)
Q	mass flow rate ($kg\,s^{-1}$)
r	droplet radius (m)
R	universal gas constant ($8.314\,J\,mol^{-1}\,K^{-1}$)
s	GDL water saturation
SMD	Sauter Mean Diameter (m)
SR	stoichiometric ratio
t	time (s)
T	temperature (K)
u	velocity (m)
v	volume fraction
V	volume (m^2)
x	distance (m)
y	distance (m)
W	GFC width (m)
WDO	water droplets occupation
z	distance (m)

Greek symbols

$\in$	GDL void fraction
ρ	density ($kg\,m^{-3}$)
θ	contact angle (°)
μ	viscosity ($kg\,(m\,s)^{-1}$)
ω	mole fraction
Ω	droplet area (m^2)

Subscripts and superscripts

1	GFC control volume
2	interface
3	GDL control volume
a	GDL sub-volume 3*a*
air	air
an	anode
b	GDL sub-volume 3*b*
c	GDL sub-volume 3*c*
ca	cathode
CA	control area
cap	capillary
d	droplet
e	effective
fc	fuel cell
g	gas
GDL	within GDL
gen	generation
H_2O	water
im	immobile saturation
in	initial
int	interface
l	liquid
mem	membrane
O_2	oxygen
rib	land or rib
sat	saturation
v	vapor water
◦	dry

liquid droplets) interaction at the interface between the gas diffusion layer (GDL) and the gas flow channel (GFC) of a PEMFC. On the other hand, the water management is only practically achievable through indirect control of the inlet flows properties, i.e. flow rate, humidity, pressure and temperature. Therefore, a mathematical model capable of predicting the water transport phenomena inside a PEM fuel cell electrode plays a remarkable role in investigating, designing and managing PEMFC operations.

Several authors have presented one- and multi-dimensional models to simulate the water transport within the porous media. Namely, McKay et al. [3] proposed a quasi 1D two-phase flow dynamic model to simulate electrode flooding. More detailed 1D models were presented by Pasaogullari and Wang [4,5] to investigate water concentration profile along the GDL thickness. Their study focused on GDL with and without a micro-porous layer (MPL), exploiting the simplifying unsaturated flow theory (UFT) and the more complex multi-phase mixture (M^2) formulation for the gas transport. However, in Pasaogullari and Wang's models there was the limiting assumption of zero liquid water saturation at the GDL–GFC interface. This hypothesis holds for low water production rate (i.e. low current density) and low gas humidity, it does not consider the role of water in the GFC. A similar investigation was done by Nam and Kaviany [6] with the only difference that a fixed boundary condition at the GDL–GFC interface was set to account for the presence of liquid water on this surface. In this case, the knowledge of liquid water at the GDL–GFC interface was required as an external input to perform a reliable analysis. Sun et al. [7] analyzed the influence of operating parameters (cell temperature, pressure and humidification temperature) on the through-plane liquid water transport with an approach very similar to the Nam and Kaviany's one. However, they used a fixed boundary condition of zero water flux on the GFC wall parallel to the GDL surface. Again, the effect of water concentration on the GDL surface was neglected or not properly take into account. Jiao et al. [8] presented

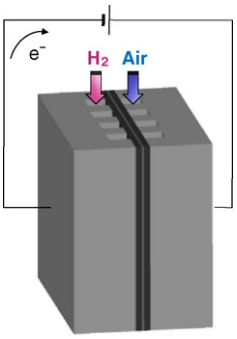

Fig. 1. Schematic of a PEMFC.

a 3D CFD model to investigate the gas and liquid flow fields in micro-channels, considering six cases for the initial liquid distribution. An analogous investigation was carried out by Sui et al. [9] but the transport equations were solved also in the electrodes and membrane. Yi et al. [10] studied the along-the-channel liquid water profile and relative scaling-up effects. On the other hand, Chen et al. [11] developed a simplified 2D numerical model of the detachment from the GDL surface of a single droplet crossed by a gas flow. A similar study was also done by Theodorakakos et al. [12], but with a much more complex CFD model. Zhu et al. [13] presented a dynamic model of a single droplet and two coalescing droplets emerging from a GDL pore. Bazylak et al. [14] showed the eruptive transport which leads to water droplets appearance on the GDL surface. Therefore, to the authors' knowledge, nothing has been published yet on a low order model suitable to describe the liquid water transport in a PEMFC, including the multi-droplets scenario at the GDL–GFC interface. The objective of this study is to embed physical description within fast simulation models. A mean value model (MVM) is developed to simulate liquid water transport phenomena in a PEM fuel cell, including polymeric membrane, the GDL media and the GDL–GFC interface.

This work is part of a broader research activity oriented towards the study and the development of control strategies whose main goal is to guarantee stable performance and lifelong operations of PEMFC. To this purpose, the model described herein will be embedded in a dynamic model developed by the authors for both PEMFC transient simulations [15,16] and related control strategies design [17].

It is important to highlight that the expected contribution of this work is in the field of PEMFC design, monitoring, control and diagnosis algorithms. As stated before, the goal of the work is to develop a model relying on the available knowledge of the phenomena affecting the water processes in a PEMFC electrode. Therefore, the proposed model is developed to be fast and reliable, as such it is not meant to substitute high order models of PEMFC electrochemistry and fluidynamics. It is implemented gathering the current knowledge of the involved phenomena present in the state-of-the-art. Nonetheless, it fills the gap in the modeling of the water droplets emergence and interaction with the air flow on the GDL surface. Furthermore, the droplet–air flow interaction is the focus of an ongoing experimental study, whose results were partially presented in a previous publication [25].

2. Modeling water transport in a PEMFC

PEM fuel cells performance is dramatically affected by water balance in the membrane. The right quantity of water is required to guarantee high proton conductivity in the polymeric membrane. Hence, a substantial amount of water inside the electrode and gas diffusion layer (GDL) is needed to keep the electrolyte at the suitable humidity level. However, an excess of liquid water in the porous media may clog the GDL micro-channels (flooding) that carry the air flow. This occurrence at the cathode side limits the oxygen diffusion towards the catalyst layer, leading to the non-operability of the fuel cell (oxygen starvation). On the other hand, a water deficit may occur for operating temperature above 75–80 °C.

As introduced above, the water transport mechanisms are complex and a low order model can only be developed if a number of simplifying hypothesis are made. In the pursuit of these research objectives, some model features are guaranteed to comply with target applications, such as unsteady process description via dynamic simulation for control strategies development. Thus, the assumptions used to model the water transport within the fuel cell are listed below:

(1) the water flux across the membrane is the balance between electro-osmotic drag and back-diffusion, while pressure driven flow is neglected since the difference between cathode and anode pressure is relatively small;
(2) the reaction water is formed in liquid phase;
(3) the reacting sites are much smaller than the GDL mean pore size, moreover they are so finely packed that the GDL surface in contact with the catalyst layer results uniformly wetted by the water formation;
(4) the net water flux in the GDL is along the through-plane direction and is capillary pressure driven;
(5) the evaporation rate in the GDL is negligible with respect to that in the GFC;
(6) the gas pressure gradient is negligible with respect to the liquid pressure gradient in the GDL;
(7) droplets emerge from the GDL with a spherical geometry (i.e. spherical calotte/segment);
(8) the droplets feeding flow is uniformly distributed;
(9) the fuel cell and the inlet streams are isotherm.

Although energy conservation has not been implemented in the current model version, water is formed in the liquid phase, but then evaporates or condensates in the gas flow channel depending on the discrepancy between current vapour and saturation pressure at the simulated temperature. Assumptions 3, 4 and 8 exclude the possibility for liquid water preferential pathways. In particular, assumption 4 is justified by the fact that the Bond number for water in the GDL is low [20]. Assumption 6 results in underestimating the porous media water saturation with respect to the case where gas pressure gradient is modeled [4].

Fig. 2 illustrates a schematic of the processes that involve liquid water at the cathode of a PEMFC. In particular, water:

- is produced on the catalyst layer by the electrochemical reaction between oxygen and hydrogen (volume 3*a* in Fig. 2);
- flows across the membrane from the cathode to the anode or vice versa depending on the operating conditions;
- flows from the catalyst layer to the GDL–GFC interface driven by a capillary pressure gradient (volume 3 in Fig. 2);
- reaches the GDL–GFC interface and forms droplets, which can either remain on the interface or are swept away by the air flow (volume 2 in Fig. 2);
- droplets standing on the interface are subject to evaporation or condensation due to the vapour partial and saturation pressure difference.

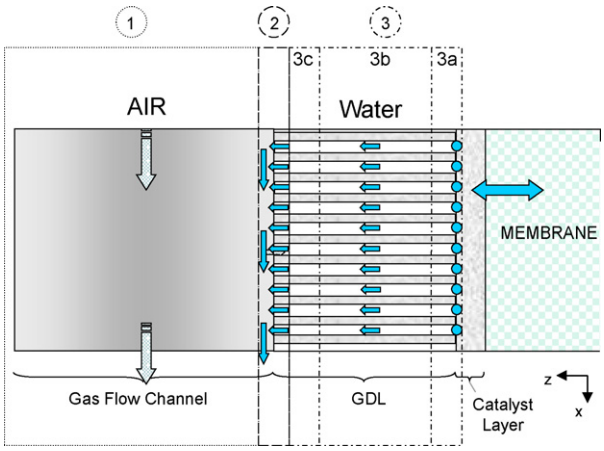

Fig. 2. Simplified scheme of water and air fluxes in a PEMFC cathode. 3*a*, 3*b* and 3*c* are the GDL control volumes, 2 is the GDL–GFC interface control area and 1 is the GFC.

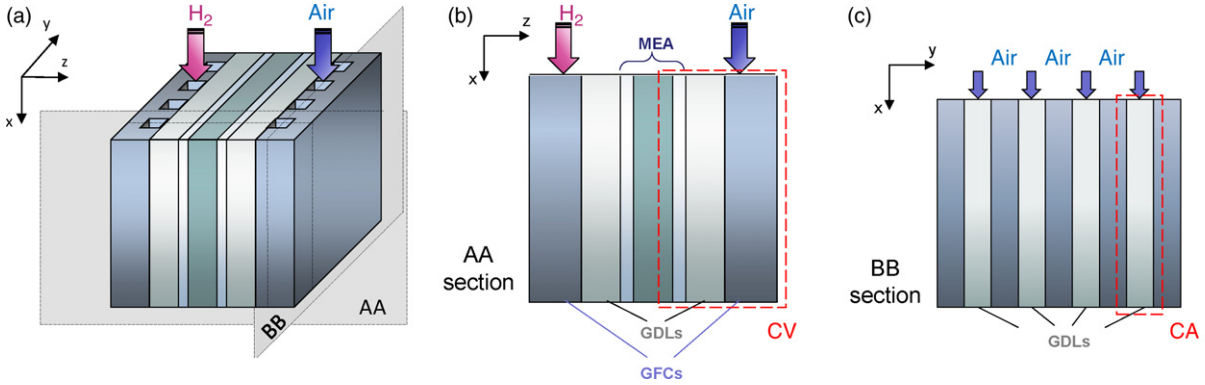

Fig. 3. (a–c) Simplified sketch of a PEMFC with sections to highlight modelling approach.

In modelling these processes, the focus has been put on the cathode since it is the most critical electrode in terms of flooding occurrence. Therefore, phenomenological models for the reaction water production and the membrane cross-flow are exploited. According to the MVM approach, the transport in the GDL is modelled by dividing its volume in three sub-volumes along the thickness (volumes 3*a*, 3*b* and 3*c* in Fig. 2). This was done to simulate boundary conditions, on one side for the reaction water (3*a*) and on the other side for the interface (3*c*).

Fig. 3 illustrates a simplified sketch of a PEM fuel cell, with a polymeric membrane in the middle and, going from the center to the sides, two catalyst layers, two GDLs and two plates with air and hydrogen flow channels (Fig. 3a). The size of the components is out of scale as the drawing is meant to clarify the above described modelling approach. In particular, the section on the plane AA (Fig. 3b) shows the control volume considered for the water transport in the GDL, therefore water flows through the porous media only along the *z* direction. On the other hand, the section on the plane BB (Fig. 3c) enlightens the control area of the 2D model of water droplets evolution at the GDL–GFC interface, which hence takes place on the *x*–*y* plane, as detailed in the next section. To notice that the CV highlighted in Fig. 3b corresponds to the mirrored image of the scheme provided in Fig. 1.

2.1. Membrane water cross-flow

The water flow across the polymeric membrane is calculated as the balance between two contributes, electro-osmotic drag and back-diffusion. A linear concentration profile along the electrolyte thickness is considered [3]:

$$Q_{H_2O,mem} = M_v A_{CA}(1 + A_{rib}) \left(\frac{n_{difc}}{F} - D_w \frac{C_{v,ca} - C_{v,an}}{l_{mem}} \right) \quad (1)$$

where the electro-osmotic drag coefficient n_d and the membrane water diffusion coefficient D_w are function of the membrane water content [23]. $C_{v,ca}$ and $C_{v,an}$ are the membrane water concentrations at the cathode and anode respectively. Since the focus of this sub-model is to provide only the boundary condition at the catalyst-membrane interface (see Fig. 2 volume 3*a*), a detailed description of the water transport within the membrane is not considered. Thus, the above mentioned coefficients are evaluated assuming that the membrane water content is the average between anode and cathode water contents, which in turn are directly related to the electrodes relative humidity [3]. Furthermore, the potential influence of the liquid water saturation in the GDLs is not taken into account in accordance with the available studies [3–9]. The parameter A_{CA} is the control surface area and represents the area under the open channel, while A_{rib} is the associated land (or rib) area and is expressed as percentage of the A_{CA}. They are represented by the dark and light blue regions, respectively, included in the control area sketched with a red dashed line in Fig. 3c.

2.2. Water generation

All the water generated by the electrochemical reaction is assumed to be in liquid phase. The generation rate is calculated with a static electrochemical relationship:

$$Q_{H_2O,gen} = \frac{M_v}{2F} i_{fc} A_{CA}(1 + A_{rib}) \quad (2)$$

which does not account for any kinetic effect.

2.3. GDL water flow

As illustrated in Fig. 1, the GDL volume is divided into three sub-volumes to proper simulate the water generation on one side and the GDL–GFC interface on the other side. Hence, each *i*-th volume (3*a*, 3*b* and 3*c*) is treated as a lumped volume, characterized by a different value of:

- saturation *s*, fraction of liquid water volume with respect to the GDL total pore volume:

$$s_i = \frac{V_{H_2O,i}}{V_{GDL,i}} \quad (3)$$

- void fraction, fraction of gas volume with respect to the GDL total pore volume:

$$\in_i = \in^0_{GDL}(1 - s_i) \quad (4)$$

where $\in^0_{GDL}$ is the GDL dry void fraction and the subscript $i = a, b, c$ denotes the control volumes 3*a*, 3*b* and 3*c* respectively. $V_{GDL,i}$ is the value of GDL sub-volume with respect to the GDL total pore volume V_{GDL}:

$$V_{GDL,i} = v_i V_{GDL} \quad (5)$$

hence v_i is the fraction of GDL sub-volume with respect to the GDL total volume. As proposed by several authors, for the purpose of models implementation, a reduced [3,7] or effective [20] water saturation is introduced:

$$s_e = \frac{s - s_{im}}{1 - s_{im}} \quad (6)$$

where *s* is calculated from Eq. (3) and s_{im} is the immobile saturation (usually assumed equal to 0.1), i.e. the residual saturation below which water is immobile [20].

The water mass conservation within the GDL is enforced for each control volume through the following set of equations:

$$\frac{d}{dt}m_{H_2O,a} = Q_{H_2O}^{mem} + Q_{H_2O}^{gem} - Q_{H_2O}^{a\to b} \tag{7a}$$

$$\frac{d}{dt}m_{H_2O,b} = Q_{H_2O}^{a\to b} - Q_{H_2O}^{b\to c} \tag{7b}$$

$$\frac{d}{dt}m_{H_2O,c} = Q_{H_2O}^{b\to c} - Q_{H_2O}^{c\to int} \tag{7c}$$

$m_{H_2O,i}$ is the mass of liquid water in the i-th volume, $Q_{H_2O}^{a\to b}$, $Q_{H_2O}^{b\to c}$, $Q_{H_2O}^{c\to int}$ are the flow rates between the volumes 3a and 3b; 3b and 3c; 3c and the interface. The sum $Q_{H_2O}^{mem} + Q_{H_2O}^{gem}$ represents the net flow rate going from the membrane and catalyst layer into the GDL sub-volume 3c.

The ODEs set (7a–c) is coupled with a set of algebraic equations describing the water flow inside the porous media and at the interfaces, as explained in the following sub-sections.

2.4. Capillary flow

The water transport within the GDL is modelled using the Darcy's law:

$$Q_{H_2O}^{i\to i+1} = \rho_{H_2O} A_{CA} \in_i u_{cap}^{i\leftarrow i+1} \tag{8}$$

with capillary velocity:

$$u_{cap}^{i\to i+1} = -\frac{K k_{rl}}{\mu}\left.\frac{\partial P_l}{\partial z}\right|_i \tag{9}$$

where μ is the water viscosity, K and k_{rl} are the GDL absolute and relative permeability, respectively. P_l is the liquid pressure, which is related to the capillary pressure P_{cap} as follows:

$$P_{cap} = P_l - P_g \tag{10}$$

Under the assumption of constant gas pressure: $(\partial P_{cap}/\partial z) \cong (\partial P_l/\partial z)$. Following the MVM approach, the capillary pressure gradient is computed as:

$$\left.\frac{\partial P_{cap}}{\partial z}\right|_i \cong \frac{P_{cap,i+1} - P_{cap,i}}{v_i l_{GDL}} \tag{11}$$

where l_{GDL} is the GDL thickness. In the available literature, most of the GDL numerical models are based on the Leverett approach to find a relationship between capillary pressure and water saturation. However, this approach was developed for a fluid permeating an isotropic soil, but the GDL of a PEMFC is rather anisotropic, either because of the 3D voids distribution and the treatment with hydrophobic material. Therefore, the capillary pressure-saturation function used in this study is a modified Leverett approach proposed by Kumbur et al. [18]:

$$P_{cap} = -4854.1 s_e^2 + 12958 s_e 0 < s_e < 0.8 \tag{12}$$

The relative permeability–saturation correlation was taken from the same source [18]:

$$K_{rl} = (s_e)^{2.16} \tag{13}$$

It is important to highlight that even though the relationships (12) and (13) are not general enough to hold for any type of GDL, they work well for carbon cloth and carbon paper GDLs with low PTFE content ($\lesssim$5%).

3. GDL–GFC 2D interface model

The water behavior model at the GDL–GFC interface links the water flow inside the GDL to the water–air interaction in the cathode channel. The description of these processes enables the appropriate simulation of the water management. It is important to point out that so far only few published works have tried to address this problem. For the objectives of this study, the simulation of the droplet population on the GDL surface cannot be approached with a detailed physical model. This would indeed imply the engagement of very complex approaches, as for example statistical characterization of the materials structure and droplet–air flow aeroelastic analysis. Therefore, the authors propose a phenomenological model to reproduce the involved processes starting from experimental evidence and detailed (i.e. 3D) simulation available in the literature [6–14].

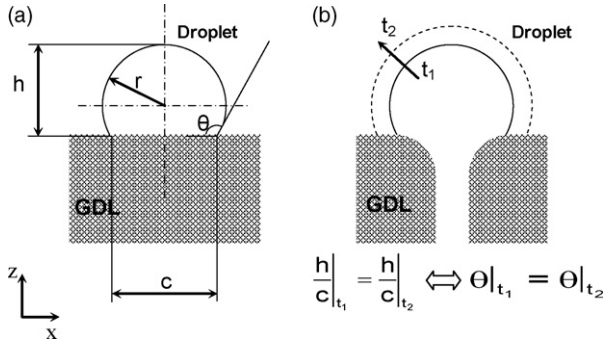

Fig. 4. Droplet growing on the GDL surface with a constant contact angle and hence height-to-chord ratio.

Fig. 4a illustrates the simplified geometry of a droplet on the GDL surface. Given the assumption of spherical symmetry, the droplet is defined by two of the four parameters height h, chord c, radius r and contact angle θ. It is worthwhile recalling that the contact angle quantifies the wetting of a solid by a liquid. It is defined as the angle formed by a drop of liquid on the solid surface at the contact line among the liquid, solid and gas. If the contact angle is less than 90° the liquid is said to be wetting, if it is greater than 90° the liquid is said to be non-wetting. In the case of a PEMFC cathode, the liquid is water, the gas is air and the solid is the GDL. The latter is often treated with hydrophobic material (PTFE) to facilitate the water removal. This is justified by the fact that the hydrophobic coating translates into contact angles greater than 90° and hence the water is non-wetting, which also means weaker adhesion force with respect to the wetting case. Thus, the water droplets on a hydrophobic surface are carried away more easily by the air in the GFC [21].

Starting from the assumptions listed at the beginning of this section, the simulation of the liquid water evolution at the GDL–GFC interface is based on the following additional hypotheses:

- the capillary velocity $u_{cap}^{c\to int}$ (i.e. water physical velocity from the volume 3c to the interface) is equal to $u_{cap}^{b\to c}$ (i.e. water physical velocity from the volume 3b to the volume 3c);
- water flows from the volume 3c to the GDL surface only when the effective saturation, s_e, in this volume is greater than the immobile saturation, s_{im}, since for lower saturation values a liquid continuous vein does not form [20];
- the initial droplets size is larger than the GDL mean pore size [12,19];
- the initial droplets position and size distribution are random;
- droplets grow with a constant height-to-chord ratio, the contact angle is constant and depends only on the GDL surface properties (Fig. 4);
- touching droplets merge into one larger droplet, whose mass is the sum of the droplets mass and position is the center of mass of the droplets (Fig. 5);

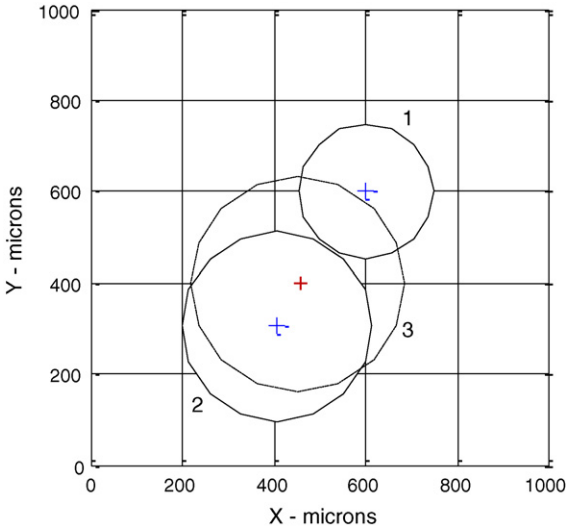

Fig. 5. Coalescing process between two droplets 1 and 2 into a bigger droplet.

- the interaction of the upstream droplets with the air flow does not affect the interaction of the downstream droplets with the air flow;
- droplets in contact both with the side-walls of the GFC and the GDL behave as droplets in contact with the GDL only;
- droplets in contact only with the GFC walls exit the surface control area instantaneously;
- droplets detach from the GDL surface because of the interaction with the air flow and the critical size for detachment follows a hyperbolic law [19,22];
- any 3D effect, such as contact with top wall, presence of turns, formation of slugs, clogs is discarded.

In summary, the GDL–GFC interface 2D model predicts the formation of droplets on the GDL surface from the water emerging from the GDL pores. The initial size of the droplets is greater than the GDL mean pore size due to the larger surface openings as experimentally observed by Kumbur et al. [19] and Theodorakakos et al. [12]. This is attributable to the presence of rounded edges, as sketched in Fig. 4b. Fed by the capillary flow, the droplets grow with a constant height-to-chord ratio (Fig. 4b), which means that the contact angle is constant as well. Droplets coalescence is also simulated as shown in Fig. 5, where two droplets 1 and 2, on a 1 mm × 1 mm GDL surface, come into touch at the time t and coalesce into a lager droplet 3 at the time $t+dt$. During the merging process, the mass is conserved and the center of the resulting droplet is in the center of mass of the two starting droplets. When a droplet reaches critical size for detachment, the air crossing-flow carries it away. Detached droplets can follow a complex trajectory, usually over the more hydrophilic side-walls. However, the simulation of this process goes beyond the objectives of this study. The droplet detachment size is function of the GDL material and the air velocity [19,22]. In this model, the detachment size – and the detached droplet velocity – air velocity relationships are derived from the experimental data published by the authors [25], which also allows to account for the air-induced droplet deformation that is not directly modeled herein.

When the air flow crosses a droplet, wakes are generated and the downstream air flow could cross other droplets before becoming steady-state again. This effect can be simulated with complex fluidynamic models of the local gas stream properties. Therefore, they can be embedded in a low order model only if synthesized into simplified models with some parameters, that for instance could be derived experimentally as the authors have done for the detachment.

The population of droplets on the GDL surface is described with three variables, the number of droplets (N_{drops}), the water droplets occupation (WDO) and the Sauter Mean Diameter (SMD). WDO is the fraction of GDL surface under the open channel covered by the droplets, while SMD is calculated as the ratio between the sum of volumes and the sum of surface areas of all droplets. Both WDO and SMD are computed exploiting the assumption of droplets with spherical geometry.

Modeling the water preferential pathways through the GDL with a deterministic approach is only feasible with CFD and several assumptions on the material structure. However, this deterministic knowledge goes beyond the objectives of this work, hence the initial droplets position and size distribution are set randomly. It is important to notice that, fixed an operating condition, a high number of simulations for different position and size distributions led to the same steady-state value of the interface variables.

3.1. Channel flow

The air flow rate required by the fuel cell to work at a given current density is modeled with a static relationship similar to Eq. (2):

$$Q_{\text{air}} = \frac{M_{\text{air}}}{4F\omega_{O_2}} i_{\text{fc}} A_{\text{fc}} \text{SR} \tag{14}$$

where SR is the air-to-hydrogen ratio (stoichiometric ratio) and A_{fc} is the active area of a reference fuel cell. Therefore, the air velocity inside the GFC is:

$$u_{\text{air}} = \frac{Q_{\text{air}}}{\rho_{\text{air}} HWN} \tag{15}$$

where H and W are the channel height and width, respectively. N is the number of GFC in parallel, or, in other words, the number of streams the overall air flow rate is split into.

3.2. Evaporation/condensation rate

The water droplets that are at the GDL–GFC interface are subject to evaporation or condensation as a consequence of the difference between the vapor partial and saturation pressure in the air flow at the given temperature. Considering forced convection as the dominating mechanism of mass transfer between liquid and gas phase, the rate of evaporation/condensation for a single droplet can be calculated as:

$$Q_{H_2O}^{\text{evap}} = \frac{K_m A_d}{R_v T_{\text{fc}}} (P_{\text{sat}} - P_v) \tag{16}$$

where the droplet cross-sectional area, A_d, is a function of time. The mass transfer coefficient, k_m, can be estimated with the use of dimensionless groups such as the Sherwood, Schmidt and Reynolds number. Since a relationship for the hereby modeled problem is not available, the correlation for flow past a submerged sphere is exploited [24].

3.3. Droplets population

As mentioned above, the water flows from the volume 3c to the interface with a velocity $u_{\text{cap}}^{b\to c}$ only if the water saturation in this volume is greater than the immobile saturation. Thereafter, droplets are formed on the GDL surface with random position and size distribution. Each droplet is then tracked in a geometrical fashion (sphere segments and calottes) and an overall mass conservation

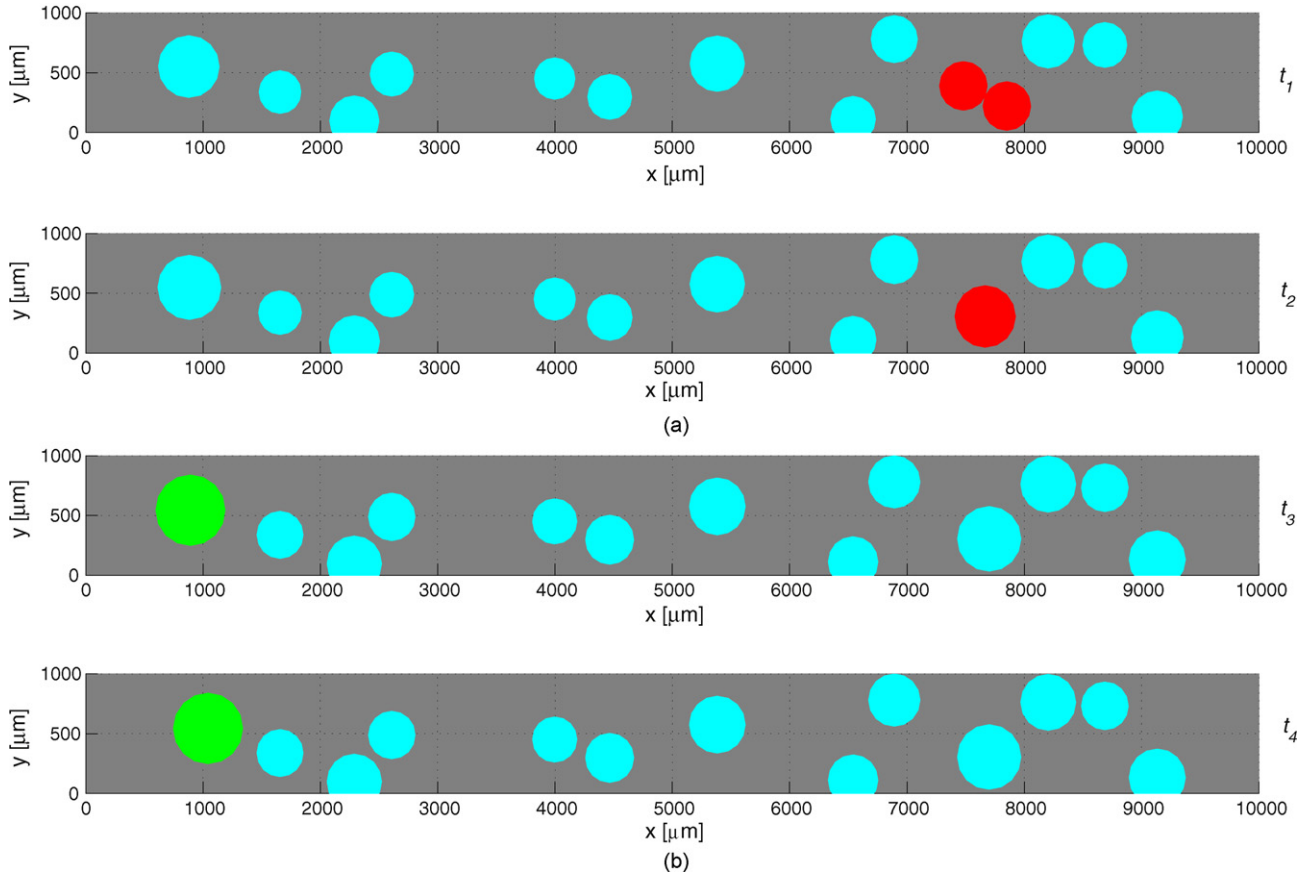

Fig. 6. Frames of the 2D model of the interface with coalescing droplets in red (a) and a detached droplet in green (b). (For interpretation of the references to color in the citation of this figure, the reader is referred to the web version of the article.)

is enforced with the following equation:

$$\frac{d}{dt}m_{H_2O,int} = Q_{H_2O}^{c\to int} - Q_{H_2O}^{evap} - Q_{H_2O}^{out} \tag{17}$$

where $m_{H_2O,int}$ is the total mass of water droplets:

$$m_{H_2O,int} = \sum_{N_{drops}}^{N_{drops}} m_{d,i} \tag{18}$$

$Q_{H_2O}^{C\to int}$ is the capillary flow rate from the GDL to the interface with the GFC (Eq. (8)) and feeds all the droplets uniformly. $Q_{H_2O}^{evap}$ is the total droplet evaporation flow rate, i.e. the sum of the single droplets evaporation flow rate as in Eq. (16):

$$Q_{H_2O}^{evap} = \sum_{i=1}^{N_{drops}} Q_{d,i}^{evap} \tag{19}$$

$Q_{H_2O}^{out}$ is the droplet flow rate that exit the control surface area because of the air drag. It is evident that Eq. (17) can be solved only if the initial droplet position and size distributions are known, from here the necessity of setting random initial distributions.

Besides growing, coalescing and evaporating/condensing, the droplets can also detached when critical size is reached, which is related to the air velocity with the following law [25,26]:

$$h_c = 6.948u_{air}^{-0.927} + 0.338 \tag{20}$$

where h_c is the droplet critical size for detachment in millimeters. Detached droplets are swept by the air velocity according to another empirical relationship derived from the experimental data presented in [25,26]:

$$u_d = 0.0021u_{air}^2 - 0.0035u_{air} + 0.0844 \tag{21}$$

It is worth noticing that Eqs. (20) and (21) could be replaced by a more detailed model describing the droplet detachment process. This has to account for droplet oscillation before detachment [26] and air drag versus adhesion force for running droplets. These processes are the topics of an ongoing study of the authors.

Coalescence between droplets is modeled as mentioned above. In particular, for the droplets sketched in Fig. 5, the mass of the droplet 3 resulting from the merging of droplets 1 and 2 is:

$$m_{d,3} = m_{d,1} + m_{d,2} \tag{22}$$

and its position is:

$$x_{d,3} = \frac{x_{d,1}m_{d,1} + x_{d,2}m_{d,2}}{m_{d,1} + m_{d,2}} \tag{23a}$$

$$y_{d,3} = \frac{y_{d,1}m_{d,1} + y_{d,2}m_{d,2}}{m_{d,1} + m_{d,2}} \tag{23b}$$

However, since coalescence does not have a direct impact on the water total mass, it is hidden in each term of Eq. (17) as N_{drops} changes.

Finally, the droplets population is described with three variables, total number of droplets N_{drops}, water droplet occupation (WDO):

$$WDO = \frac{\sum_{i=1}^{N_{drops}} \Omega_{d,i}}{A_{CA}} \tag{24}$$

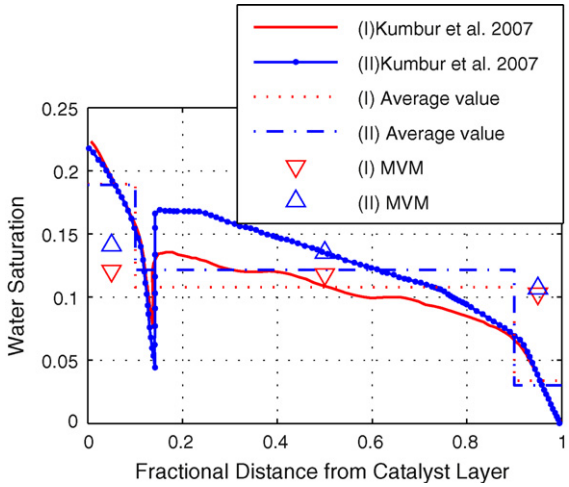

Fig. 7. Comparison with numerical results of Kumbur et al. [18] for two types of GDL carbon paper, I = TORAY090, II = SGL10BA. Relative error values are indicated.

where $\Omega_{d,i}$ is the patch area of the i-th droplet, and Sauter Mean Diameter:

$$\mathrm{SMD} = \frac{\rho_{H_2O} m_{H_2O,\mathrm{int}}}{\sum_{i=1}^{N_{\mathrm{drops}}} (A_{d,i} + \Omega_{d,i})} \tag{25}$$

4. Results and discussion

In this section a set of results is presented to assess the numerical model. Simulations are performed for steady-state conditions and compared with data published in the literature. Furthermore, since the model includes several parameters, which are summarized in Table 3, simulations are run to investigate the effect of some of these parameters.

4.1. Droplet population tracking

A graphical tool that returns images of the droplet population on the GDL surface is implemented in the 2D model of the interface. Fig. 6 shows consecutive frames generated by the code. In particular, in Fig. 6a coalescing droplets are illustrated in red, at the time instant t_1 a pair of droplets is touching and at t_2 they have merged into one larger droplet. In Fig. 6b at the time instant t_3 the droplet highlighted in green reaches detachment size (about 600 μm) and at t_4 it has traveled some distance.

4.2. Model assessment

The first comparison is made with the numerical results published by Kumbur et al. [18], whose modified Leverett approach and relative permeability formula are exploited in this work (see Eqs. (12) and (13)). Fig. 7 illustrates the comparison of results obtained for two types of GDL material, i.e. Toray® 090 (0% PTFE) and SGL® 10BA (5% PTFE) carbon paper; the reader is addressed to the referential paper for further material specifications. For the purpose of comparing the two models, the one-dimensional saturation profile is divided into three parts in accord with the three GDL sub-volumes of the authors' model. The saturation values are averaged over the volumes used in the simulation and are compared with the MVM results; the calculated relative errors are listed in Table 1. It may be noticed that the agreement is fairly good in the middle sub-volume, but is poor in the outer sub-volumes. This is explainable analyzing the differences between the two models. As for the left outmost part, the MVM does not simulate the presence of a micro-porous layer (MPL) as Kumbur et al.'s model does, this leads to a prediction of a lower saturation level by the MVM with respect to the referential model. On the other hand, the saturation in the right outmost sub-volume is influenced by the water at the GDL–GFC interface. Since Kumbur et al.'s model sets zero liquid water at this interface, the saturation level in the volume next to it is lower than the case where liquid water is considered as done in the current work. This comparison cannot be regarded as a model validation because of the above evidenced discrepancies. As a matter of fact, the porous media structure (GDL + MPL) and boundary conditions adopted by the referential work are not fully reproducible with the current version of the MVM.

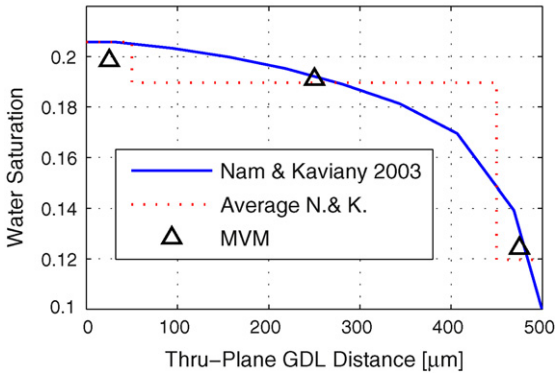

Fig. 8. Comparison with numerical results of Nam and Kaviany [6]. Relative error values are indicated.

A more consistent comparison is carried out with the 1D model presented by Nam and Kaviany [6] as shown in Fig. 8; where the plotted items are analogous to those explained for Fig. 7. The rela-

Table 1
Relative errors for the comparison with numerical results of Kumbur et al. [18].

Sub-volume	Relative error [%]	
	I	II
3*a*	−36.3	−25.2
3*b*	9.45	11.2
3*c*	203	254

Table 2
Relative errors for the comparison with numerical results of Nam and Kaviany [6].

Sub-volume	3*a*	3*b*	3*c*
Relative error [%]	−3.61	0.67	3.80

Table 3
Model parameters baseline values.

Parameter	Value
P_{air} air pressure	1 bar
T_{fc} temperature	353 K
SR stoichiometric ratio	2
RH_{ca} cathode relative humidity	80%
RH_{an} anode relative humidity	80%
i_{fc} current density	1 A cm^{-2}
N number of GFC in parallel	4
H GFC height	1 mm
W GFC width	1 mm
A_{fc} active area	225 cm^2
A_{CA} control area	0.1 cm^2
A_{rib} land area	50%
l_{GDL} GDL thickness	300 μm
ϵ^0_{GDL} GDL dry void fraction	74%
K absolute permeability	10^{-12} m^2
θ_{GDL} GDL contact angle	130°
v_a, v_b, v_b GDL sub-volume fractions	0.1, 0.8, 0.1
D_{in} initial droplet size	100 μm

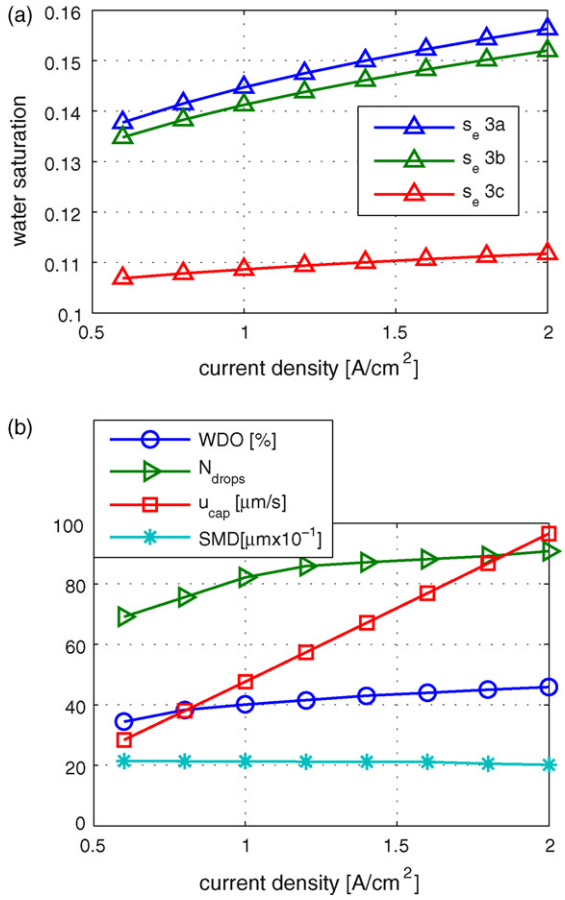

Fig. 9. MVM sensitiveness to the current density. (a) Water saturation in the sub-volumes and (b) interface water occupation, droplets number, capillary velocity and droplets Sauter Mean Diameter.

tive errors between the referential work and the MVM are listed in Table 2. The good agreement between the water saturation values points out the fairness of the proposed MVM approach. Furthermore, this highlights the correctness of the hypotheses assumed for the implementation of the saturation values in the region next to the GDL–GFC interface. It is worthwhile noticing that Nam and Kaviany's model does not simulate explicitly the water evolution at the GDL–GFC interface, but simply accounts for a non-zero boundary condition, whereas the amount of water at this interface is computed with the MVM.

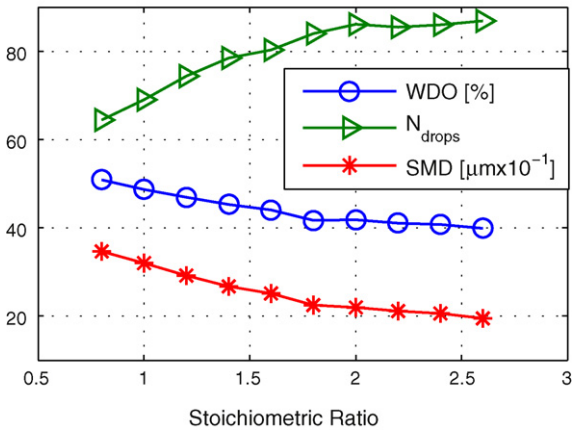

Fig. 10. Change in interface water occupation, droplets number, and droplets Sauter Mean Diameter with stoichiometric ratio.

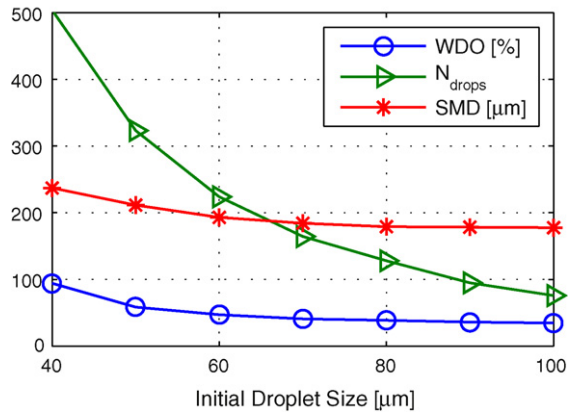

Fig. 11. Influence of the initial droplets diameter on the water occupation, droplets number and Sauter Mean Diameter.

4.3. Parametric study

In order to judge the physical consistency and the sensitiveness to the parameters of the MVM, a parametric study is performed. Therefore, some parameters are changed one at a time, starting from the baseline values tabulated in Table 3.

The influence of the current density on the variables within the GDL and at the GDL–GFC interface is represented in Fig. 9. In particular, in Fig. 9a the steady-state saturation inside the three

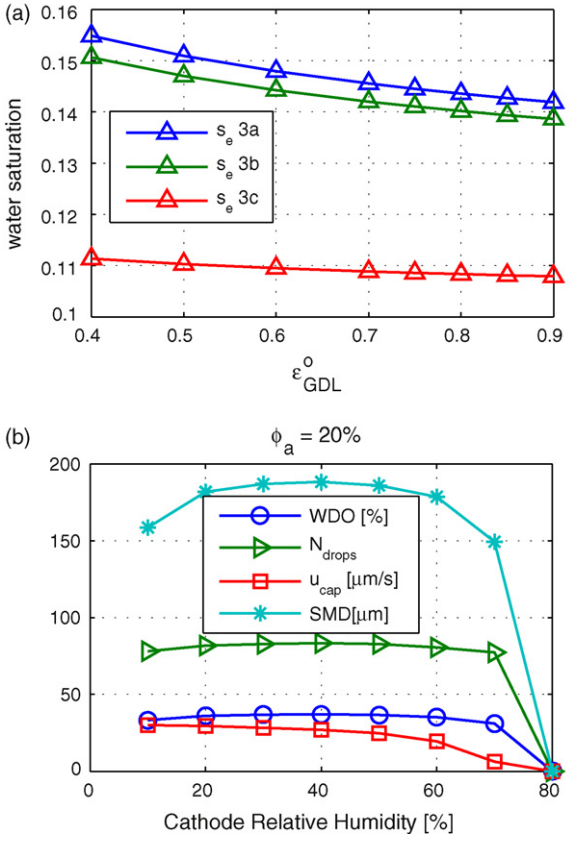

Fig. 12. Sensitiveness of the MVM to the GDL dry void fraction. (a) Water saturation in the sub-volumes and (b) WDO, droplets number, capillary velocity and droplets SMD.

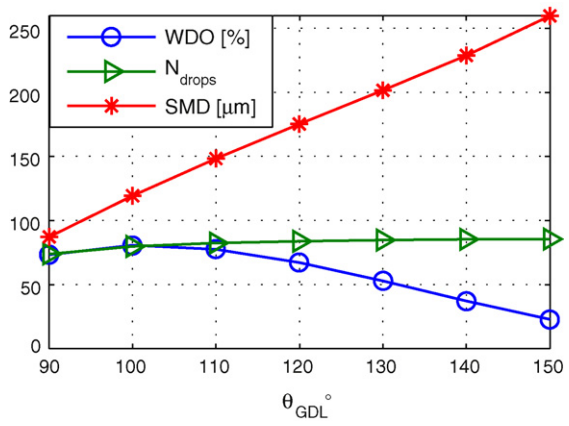

Fig. 13. Influence of the GDL contact angle on the WDO, droplets number and SMD.

GDL sub-volumes increases as the current density is increased, as expected. The time average of the water droplets occupation of the surface at the GDL–GFC interface is plotted in Fig. 9b. In this figure, the time average of both the number of droplets on the surface and their Sauter Mean Diameter and the capillary velocity $u_{cap}^{c\to int}$ are displayed. The capillary velocity exhibits a linear behavior with the current density, while the number of droplets and the *WDO* increase increases with a power law. Therefore, as expected from physical reasoning, as the current density increases, more droplets form on the interface, but they have a smaller average size since the Sauter Mean Diameter decreases. This is because the droplet critical size for detachment is smaller for higher air velocity, i.e. higher current densities (see Eq. (15)).

The model sensitiveness to the stoichiometric ratio SR is investigated by keeping constant load current as reported in Fig. 10, where the time average of the water occupation and the droplets size (i.e. Sauter Mean Diameter) decrease significantly when SR increases since higher air velocity carry away the droplets more easily. On the other hand, the increase in droplets average number with SR is justified by the increment of the decrease in the critical detachment size. This means that increasing the air velocity (i.e. SR) leads to a scenario with more droplets on the GDL surface with a smaller size.

Fig. 11 shows the influence of the initial droplets diameter on the water evolution at the GDL–GFC interface. This is quantified with the time average of the water occupation, droplets number and SMD. It can be noticed that the smaller the initial droplets size

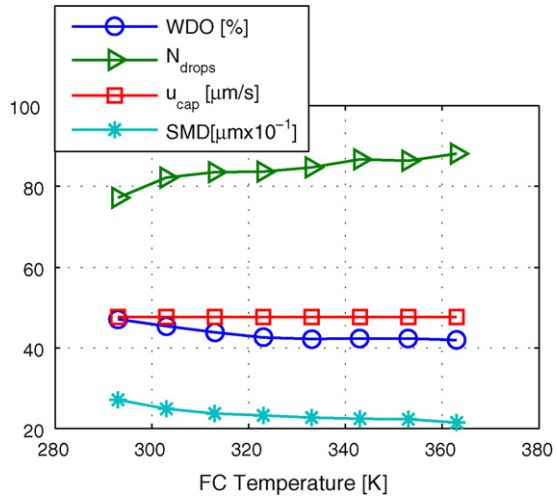

Fig. 14. Influence of fuel cell temperature on the variables of the interface.

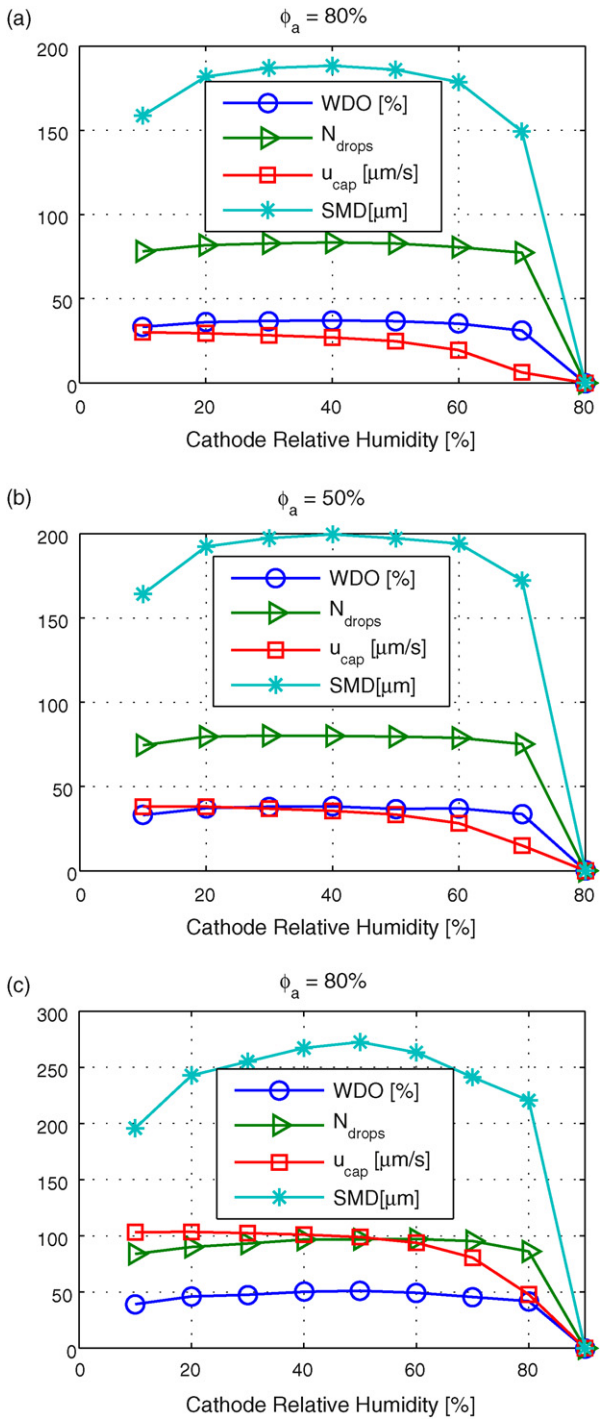

Fig. 15. (a–c) Influence of anode and cathode humidity on the droplet population evolving on the surface of the cathode GDL.

the higher the number of droplets existing on the interface and their occupation.

The GDL dry void fraction affects both the water transport inside the GDL and on the GDL surface as illustrated in Fig. 12. In particular, as the void fraction decreases the water saturation as well as the capillary velocity increases because the volume available to the passage of water is smaller (see Eqs. (3) and (8)), which is also the reason behind the use of an MPL. The values of WDO and droplets number, averaged over time, increase with the dry void fraction (Fig. 12b) since also the GDL void surface area, which is responsible for droplets formation, increases with this parameter.

The MVM sensitiveness to the contact angle of the water droplets on the GDL surface is analyzed in Fig. 13. The water occupation of the GDL–GFC interface decreases as the contact angle increases, which confirms that a more hydrophobic GDL material results in favorable water removal. Furthermore, larger contact angles produce higher numbers of droplets with smaller SMD.

The effect of temperature on the interface variables is investigated in Fig. 14. As the temperature rises the evaporation rates increases, resulting in a decrease in WDO and SMD, while the number of droplets increases. However, the influence of temperature is rather weak because of the unavailability of some model parameters as function of temperature, such as GDL permeability, contact angle.

The relative humidity of the air flow at the two electrodes has impact on the evaporation rate as well as on the membrane water cross-flow. The variation of the variables of the cathode interface with cathode and anode relative humidity is explored in Fig. 15, where the steady-state values are plotted as functions of cathode relative humidity, while the anode relative humidity is parameterized. For anode relative humidity ranging between 20 and 90%, the behavior of the droplet population on the GDL surface is similar. When cathode humidity is increased from 10 up to 50%, the number of droplets augments, which causes a higher coalescence rate, resulting in an increasing SMD. When cathode humidity goes from 50 to 70%, the effect of water diffusion from cathode to anode is predominant over the effect of coalescence, therefore the number of droplets diminishes and the SMD increases. It is important to notice that the MVM predicts that when cathode relative humidity reaches 80% and the anode one is 20 or 50%, all the water is transported from cathode to the anode, causing dehydration of the cathode. When the anode relative humidity is set to a value of 80%, the cathode dry out happens for a cathode relative humidity of 90%.

5. Conclusion

In this paper, a lumped model for the simulation of the water flow in a PEM fuel cell cathode has been presented. The model is based on a mathematical description of the capillary driven water flux within the GDL porous media and embeds an original representation of the water behavior at the GDL–gas flow-channel interface. Moreover, a sub-model of the water droplets formation on this interface and their removal by the gas stream is implemented. Such features allow computing the number of water droplets and the amount of water present on the GDL surface. Thus, by modeling these processes a reliable water management simulation is achievable. Thanks to the low computational burden of the mean value approach followed, the model is suitable for both fuel cell design and control strategies development studies.

The model accuracy has been evaluated by comparing the simulation results with respect to steady-state data available from accurate numerical analyses. Satisfactory matching has been found for in-GDL water saturation levels. A parametric analysis has been also presented to examine the influence of both GDL properties and operating parameters. Furthermore, fuel cell current step transients have been simulated to reproduce the complex interaction between water and air.

Acknowledgments

Fruitful discussions with Dr. Sandip Mazumder and the support to this work by Mr. Aaron Montello and Pierpaolo Polverino are gratefully acknowledged. The authors would also like to thank the University of Salerno and the Center for Automotive Research and the Ohio State University for providing the opportunity for this collaborative work.

References

[1] M.A. Kannan, V.P. Vinod, L. Munukutla, M.N. Ghasemi-Nejhadb, Electrochemical and Solid-State Letters 10 (3) (2007) B47–B50.
[2] J.M. Tang, M.E. Itkis, C. Wang, X. Wang, Y. Yan, R.C. Haddon, Micro & Nano Letters 1 (2006) 62–65.
[3] D.A. McKay, W.T. Ott, A.G. Stefanopoulou, Proceeding of IMECE–2005 (IMECE2005-81484), November 2005, 2005.
[4] U. Pasaogullari, C.-Y. Wang, Electrochimica Acta 49 (2004) 4359–4369.
[5] U. Pasaogullari, C.-Y. Wang, Journal of the Electrochemical Society 152 (2) (2005).
[6] J.H. Nam, M. Kaviany, International Journal of Heat Mass Transfer 46 (2003) 4595–4611.
[7] H. Sun, H. Liu, L.J. Guo, Journal of Power Sources 143 (2005) 125–135.
[8] K. Jiao, B. Zhou, P. Quan, Journal of Power Sources 157 (2006) 226–243.
[9] P.C. Sui, S. Kumar, N. Djilali, Journal of Power Sources 180 (2008) 410–422.
[10] J.S. Yi, J.D. Yang, C. King, American Institute of Chemical Engineers Journal 50 (2004), doi:10 1002/aic.10307, No. 10.
[11] K.S. Chen, M.A. Hickner, D.R. Noble, International Journal of Energy Research 29 (2005) 1113–1132.
[12] A. Theodorakakos, T. Ous, M. Gavaises, J.M. Nouri, N. Nikolopoulos, H. Yanagihara, Journal of Colloid and Interface Science 300 (2006) 673–687.
[13] X. Zhu, P.C. Sui, N. Djilali, Journal of Power Sources 172 (2007) 287–295.
[14] A. Bazylak, D. Sinton, N. Djilali, Journal of Power Sources 176 (2008) 240–246.
[15] I. Arsie, A. Di Domenico, C. Pianese, M. Sorrentino, Transaction of the ASME - Journal of Fuel Cell Science and Technology 4 (2007) 261–271, ISSN 1550-624X.
[16] A. Di Domenico, A. Esposito, Y.G. Guezennec, A. Miotti, Proceedings of ASME 2006 The 4th International Conferences on Fuel Cell Science, Engineering and Technology, June 19–21, 2006, Irvine, California, USA, 2006.
[17] I. Arsie, A. Di Domenico, C. Pianese, M. Sorrentino, Journal of Fuel Cell Science and Technology 7 (2010), 011004-011015.
[18] E.C. Kumbur, K.V. Sharp, M.M. Mench, Journal of Power Sources 168 (2007) 356–368.
[19] E.C. Kumbur, K.V. Sharp, M.M. Mench, Journal of Power Sources 161 (2006) 333–345.
[20] K. Promislow, J. Stockie, B. Wetton, Royal Society of London Proceedings Series A 462 (2067) (2006) 789–816.
[21] J.C. Berg, Wettability, Marcel Dekker, N.Y., 1993.
[22] T. Ous, C. Arcoumanis, Journal of Power Sources 173 (2007) 137–148.
[23] S.S. Dutta, J.V. Zee, International Journal of Heat and Mass Transfer 44 (2001) 2029–2042.
[24] R.H. Perry, W. Green, "Perry's Chemical Engineers' Handbook", seventh ed.
[25] A. Esposito, A. Montello, C. Pianese, Y.G. Guezennec, Proceeding of FuelCell2009 (FuelCell2009-85166), June 2009, 2009.
[26] A. Esposito, A.D. Montello, C. Pianese, Y.G. Guezennec, Journal of Power Sources 195 (2010) 2691–2699.